POAC'15
Trondheim, Norway

Proceedings of the 23rd International Conference on
Port and Ocean Engineering under Arctic Conditions
June 14-18, 2015
Trondheim, Norway

IMAGING SEA ICE STRUCTURE BY REMOTE SENSING SENSORS

Torbjørn Eltoft[1,3], Anthony P. Doulgeris[1], Camilla Brekke[1], Stian Solbø[3], Sebastian Gerland[2], and Alfred Hanssen[4]

[1]University of Tromsø, The Auroral Observatory, 9037 Tromsø, Norway.
[2]Northern Research Institute, Norway
[3]Norwegian Polar Institute, FRAM centre, 9296 Tromsø, Norway
[4]Aker Solutions, Tromsø

ABSTRACT

This paper will investigate how new developments in remote sensing and sensor technologies can be applied to image the structure of the sea ice surface. Both segmentation of multi-polarimetric synthetic aperture radar images and strategies for the analyses of polarimetric SAR data of sea ice are addressed. The analysis is based on a Radarsat 2 PolSAR scene of from the Fram Strait in September 2011. It is shown that the segmentation algorithm clearly enables segmentation of sea ice into proper segments. The paper also includes some preliminary results from a very new model-based polarimetric decomposition approach, which uses higher-order statistics to estimate the model parameters. The results are very promising for sea ice applications. Finally, using data collected in the Fram Strait with an RPAS flown out from the Norwegian Coast Guard Vessel KV Svalbard in spring 2013, it is shown that the sea ice surface structure may be adequately imaged using stereoscopic optical imaging from an RPAS platform.

INTRODUCTION

In recent years, the availability of remote sensing data has dramatically improved. New operational and science-driven missions carry sensor packages which include multi-polarization and fully polarimetric Synthetic Aperture Radars (SARs), hyper-spectral imagers, improved passive-microwave radiometers, multi-angular spectro-radiometers, spaceborne laser altimeters, and new generation radar altimeters (onboard ESAs CryoSat mission). These new technologies are improving our ability to observe sea ice properties over larger areas, as well as to obtain detailed small scale information.

For detailed sea ice studies, SAR sensors have demonstrated an immense potential. Being an imaging sensor with a variety of modes, SAR sensors can provide quantitative measurements of key parameters ranging from a few meters to hundreds of kilometers [1]. SAR images can give detailed information to help study variability and ice processes, but the interpretation of sea ice signatures is often a challenge due to the unpredictable and complex nature of backscatter from different ice types [2]. The emergence of dual-polarization and fully polarimetric (quad-pol) space-borne SAR systems gives prospects for enhancement of the amount of information about sea ice properties that can be obtained from satellite borne sensors. A system is denoted fully

polarized if it simultaneously measures all combinations of linear polarizations, i.e. VV, VH, HH, and HV, providing intensities and relative phases.

The focus in this paper is on radar remote sensing using polarimetric synthetic aperture radar imaging. Specifically, we address the potential of creating reliable sea ice type classifications, which display deformation and surface structure. The analysis will be demonstrated using a quad-pol C-band image collected by the Canadian satellite Radarsat 2 over an area in the Fram strait in September 2011.

In recent years, there has also been considerable interest in using Remotely Piloted Airborne Systems (RPAS) carrying imaging sensors for remote sensing of sea ice. These systems allow for very detailed mapping of the sea ice surface on a local scale. We will also include some preliminary results using stereoscopic optical imaging from an RPAS to create 3-D images of the sea surface. The data was collected in the Fram Strait with an RPAS flown out from the Norwegian Coast Guard Vessel KV Svalbard in spring 2013.

The paper is organized with the next two sections giving some preliminaries on the physics of sea ice and SAR polarimetry, followed by sections on the image segmentation and decomposition algorithms, and finally the RPAS mapping results. We conclude with a brief summary.

SEA ICE PRELIMINARIES

Sea ice can be divided into two major categories, first-year ice (FY) and multi-year ice (MY). MY-ice has survived at least one summer melt and is discriminated from FY-ice on the basis of properties such as deformation (roughness, surface topography), thickness, salinity and snow cover.

Sea ice is subject to constant changes due to drift and deformation. The motion is caused by forces from wind and ocean currents, and influenced by obstacles such as islands and coastlines and by ice thickness and roughness variations. The most commonly referred sea ice types are level ice, deformed ice, rafted ice, ridged ice, and hummocked ice. Level ice is ice with a relatively flat surface, which has not been deformed to any extent. Deformed ice is a general term for ice forced upwards and downwards. Rafted, ridged, and hummocked ice are subdivisions of deformed ice. Rafting arises when ice sheets collide and override one another. A ridge is the result of such processes and can be described as a long line of piled up, cracked ice. Ridging is a result of compressional and shearing interactions between ice floes. Repeated ridging causes rubble fields. Pressure processes cause the ice to pile up both above and below the surface.

Leads are open water channels in areas of predominantly sea ice. In addition to deformation characteristics there exist several ice types representing young and thin sea ice.

The extent of deformation is exploited when trying to segment a sea ice SAR scene into homogeneous regions, and subsequently discriminate between ice types.

RADAR POLARIMETRY PRELIMINARIES

Radar polarimetry is an advancing technology, which is getting increasing attention in various application areas of radar remote sensing. Polarimetry deals with the full vector nature of electromagnetic waves. General introductory texts on radar and SAR polarimetry are found in e.g. [3, 4, 5]. Changes in the index of refraction, as a consequence of changes in permittivity,

magnetic permeability, or conductivity, cause the polarization state of an electromagnetic wave to be transformed, and the electromagnetic wave vector is re-polarized. When the wave passes through a medium of changing index of refraction, or when it strikes an object or a scattering surface and it is reflected, the characteristic information about the reflectivity, shape and orientation of the reflecting body can be obtained by polarimetric analysis of the echoes [5]. This information is only available if the radar system has full polarimetric capability. For the linear polarization basis, this means the system is able to measure the backscattered signal in four polarization channels. This is mathematically formulated by means of the Sinclair matrix (also referred to as the scattering matrix), which relates the backscattered wave vector to the incident wave vector, as shown in (1) below

$$\begin{bmatrix} E_h^s \\ E_v^s \end{bmatrix} = \frac{\exp(jkr)}{r} \begin{bmatrix} S_{HH} & S_{HV} \\ S_{VV} & S_{VH} \end{bmatrix} \begin{bmatrix} E_h^i \\ E_v^i, \end{bmatrix} \tag{1}$$

where k is wavenumber of the incident electromagnetic wave, r is the distance between the radar antenna and target, E_j^i and E_j^s, $j \in \{h, v\}$, denote the jth linear polarization component of the incident and scattered waves, respectively, and the entries of the S-matrix, i.e. S_{HH}, S_{HV}, S_{VV}, S_{VH}, define the channel wise complex scattering coefficients. For practical analysis of polarimetric data, the S-matrix is often vectorized; either as a lexicographic *scattering or target vector*

$$\mathbf{s} = [S_{HH}, S_{HV}, S_{VH}, S_{VV}], \tag{2}$$

or as a *Pauli scattering vector*

$$\mathbf{k} = \frac{1}{\sqrt{2}}[S_{HH} + S_{VV}, S_{HH} - S_{VV}, S_{HV} + S_{VH}, j\,(S_{HV} - S_{VH})], \tag{3}$$

where the square-root factor maintains the total backscattered power. Data in this format is denoted single look complex (SLC) data. A scattering mechanism is often defined as a normalized Pauli scattering vector, because this can be used to characterize differences in polarized wave scattering [4].

Multi-looking the $\mathbf{s}$ or $\mathbf{k}$ vectors results in the *polarimetric covariance matrix* or *coherence matrix*, defined as

$$\mathbf{C} = <\mathbf{s}\mathbf{s}^\dagger> = \frac{1}{L}\sum_{i=1}^{L} \mathbf{s}_i\mathbf{s}_i^\dagger \text{ and } \mathbf{T} = <\mathbf{k}\mathbf{k}^\dagger> = \frac{1}{L}\sum_{i=1}^{L} \mathbf{k}_i\mathbf{k}_i^\dagger, \tag{4}$$

respectively, where the superscript † refers to conjugate transpose, and L is the nominal number of looks. This data format is called multi-looked complex (MLC) data.

A sea ice surface is generally considered to fulfill the requirement of *reciprocity*, i.e. $S_{HV} = S_{VH}$. In the remainder, we will also assume *reflection symmetry*, in which case the $\mathbf{C}$ and $\mathbf{T}$ matrices take the following forms:

$$\mathbf{C} = \begin{bmatrix} C_{11} & 0 & C_{13} \\ 0 & C_{22} & 0 \\ C_{13}^* & 0 & C_{33} \end{bmatrix} \text{ and } \mathbf{T} = \begin{bmatrix} T_{11} & T_{12} & 0 \\ T_{12}^* & T_{22} & 0 \\ 0 & 0 & T_{33} \end{bmatrix} \tag{5}$$

POLSAR IMAGE SEGMENTATION

Recent developments in PolSAR image segmentation have been towards incorporating a few key features. Firstly, that they are fully automatic and un-supervised, meaning that they require no ground-truth data or user intervention, and consequently are operator independent and consistent. Secondly, they automatically determine the very important number of clusters parameter from the data itself, in a rigorous statistical manner. Thirdly, the modelling provides good class distinction with a suitably flexible non-Gaussian or textured PolSAR model, and lastly, they provide rigorous contextual smoothing with Markov random fields to make image segments cleaner and more confident. The segmentation itself lacks the actual ice type labels, and additional knowledge must be subsequently used to try to label the distinct image segments. Two main developments have occurred. One using elaborate non-Wishart models for the MLC covariance matrix data distributions and is the most statistically rigorous, but slow to compute. The other using simple extracted features, but with less rigorous statistical modelling, and resulting in some coarse approximations. The latter is, however, significantly faster and more readily open to new features or data-fusion. Both approaches are still in active development, but are mature enough for general use, and were recently compared and shown to produce similar main classes [6]. Figure 1 shows an enhanced Pauli false-colour representation of the polarimetric SAR scene of sea ice together with segmentation results from both approaches.

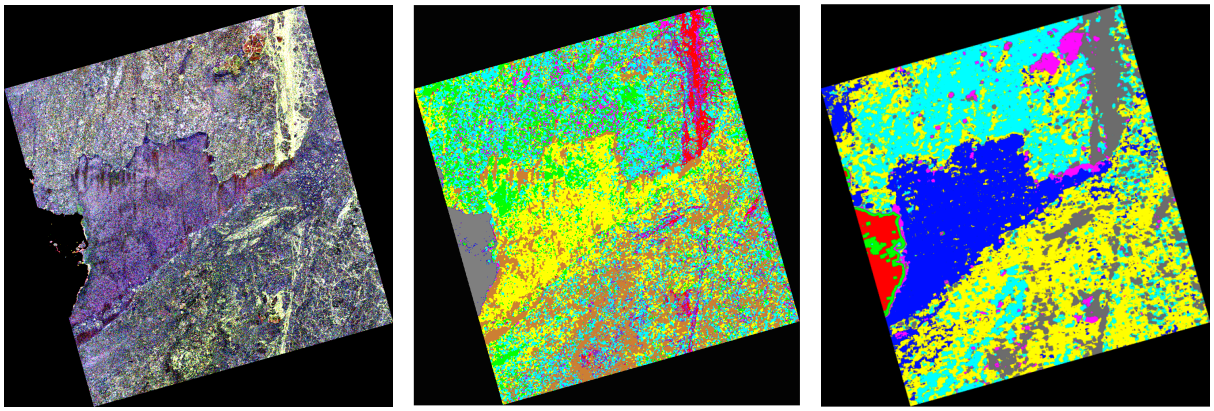

Figure 1. Images derived from the Fram Strait Radarsat 2 scene. *left:* Enhanced Pauli RGB image, *middle:* non-Wishart modelling segmentation result with 9 classes, *right:* and feature extraction segmentation result with 7 classes.

THE PAULI IMAGE

The Pauli image is a kind of coherent target decomposition. It expresses the measured scattering matrix $\mathbf{S}$ in the so-called Pauli basis. In the 3-dimensional Pauli representation, the scattering vector is, under the reciprocity assumption, defined as

$$\mathbf{k}_P = \frac{1}{\sqrt{2}}[s_{hh} + s_{vv}, s_{hh} - s_{vv}, 2s_{hv}], \tag{6}$$

where the square-root factor is used to keep the total backscattered power constant. The measured scattering matrix is then expressed as

$$\mathbf{S} = \alpha\mathbf{S}_s + \kappa\mathbf{S}_d + \gamma\mathbf{S}_v, \tag{7}$$

where

$$\mathbf{S}_s = \frac{1}{\sqrt{2}}\begin{bmatrix} 1 & 0 \\ 0 & 1 \end{bmatrix}, \mathbf{S}_s = \frac{1}{\sqrt{2}}\begin{bmatrix} 1 & 0 \\ 0 & -1 \end{bmatrix}, \mathbf{S}_s = \frac{1}{\sqrt{2}}\begin{bmatrix} 0 & 1 \\ 1 & 0 \end{bmatrix}, \tag{8}$$

and

$$\alpha = \frac{S_{HH} + S_{VV}}{\sqrt{2}}, \kappa = \frac{S_{HH} - S_{VV}}{\sqrt{2}}, \gamma = \frac{2S_{HV}}{\sqrt{2}}. \tag{9}$$

The interpretation of the Pauli decomposition is based on the definition of the individual component matrices. Matrix $\mathbf{S}_s$ corresponds to the scattering matrix of a sphere, a plate or a trihedral. In general, $\mathbf{S}_s$ is referred to single- or odd-bounce scattering. The coefficient α correspond to the contribution of $\mathbf{S}_s$ to the total scattering matrix $\mathbf{S}_s$. $|\alpha|^2$ determines the power scattered by targets characterized by single- or odd-bounce.
$\mathbf{S}_d$ represents the scattering mechanism characterized by double- or even-bounce, since the polarization of the returned wave is mirrored respect to the one of the incident wave. Consequently, κ is the complex coefficient of this scattering mechanism and $|\kappa|^2$ represents the scattered power by this type of targets.
Finally, the third matrix $\mathbf{S}_v$ corresponds to a scattering mechanism which is able to return the orthogonal polarization. This is generally interpreted to be associated with volume scattering produced by randomly oriented scattering objects. The coefficient γ represents the contribution of $\mathbf{S}_v$ to $\mathbf{S}$, whereas $|\gamma|^2$ stands for the scattered power by this type of scatterers.
Figure 2 shows to the left, the span image, and to the right, a Pauli image of a Radarsat 2 sea ice scene from the Framstrait, captured in the beginning of September 2011. . The span image dis-

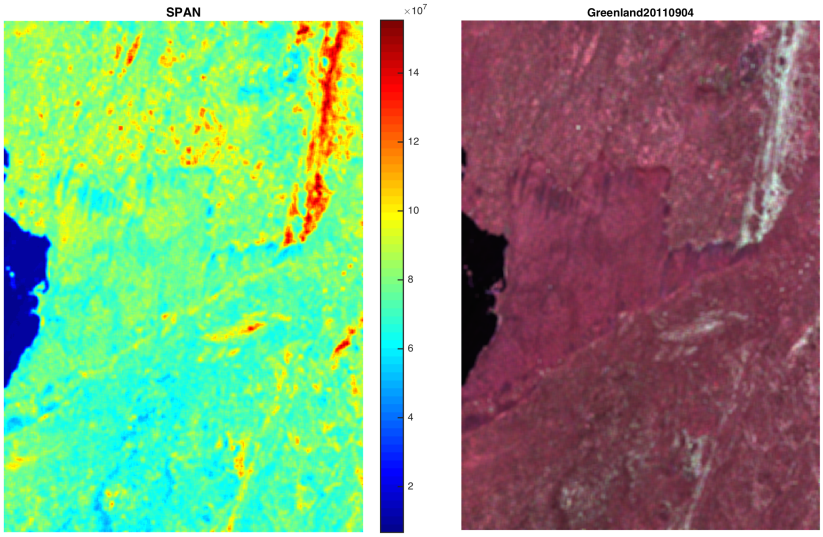

Figure 2. *Left*: Span image. *Right*: Pseudo-colored Pauli image of a Radarsat 2 sea ice scene from the Framstrait.

plays the sum of intensities in the polarimetric channels. The Pauli image is a pseudo-coloured RGB image, generated by assigning $|\kappa|^2$ to the red channel, $|\alpha|^2$ to the blue channel, $|\gamma|^2$ to the green channel, respectively. Note that the scaling of the colour coding in the Pauli image in Figure 2 is different from that in the left image in Figure 1. The image displays an area of open water to the left (black region) and various types of sea ice. By analysing the span image and the colours, we may make interpretations regarding the sea ice structure. The middle, reddish

section seems to have the relatively highest contribution of double bounce scattering. From in-situ observations, this area is believed to be a refrozen lead, and hence contains level FY ice in some stage of development. The areas above and below this section, are MY ice. In the span and the Pauli images we note more variations in the colouring and the intensity in these areas, which indicates a more complex scattering. Here we also see areas with very high intensities, which in the Pauli image have a bluish-white colour. These areas are ridged ice. Here, the scattering is strong, with a blend of contributions from all mechanisms. Finally, we note some spots of pink colour and high intensities, these correspond to chunks of icebergs.

MODEL-BASED POLARIMETRIC DECOMPOSITION

The Freeman-Durden is one of the most well-known model-based decomposition theorems [7]. It has been successfully applied to analyze polarimetric data of forest. The decomposition models the coherency matrix as the contribution of three scattering mechanisms: surface, double-bounce, and volume scattering, i.e.

$$\mathbf{T} = P_s\,\mathbf{T}_s + P_d\,\mathbf{T}_d + P_v\,\mathbf{T}_v. \tag{10}$$

The surface component is often modelled as a Bragg scattering component, $\mathbf{T}_s$, the double-bounce is a smooth dihedral reflection component, $\mathbf{T}_d$, and volume component is modelled as randomly oriented dipole scattering elements, $\mathbf{T}_v$. These component matrices are then expressed in terms of physical parameters. The Freeman-Durden method sometimes produces non-physical solutions for P_s and P_d. To avoid this, we apply a modified form, in which we only remove a fraction of the volume component, i.e., we define $\mathbf{T}_g = \mathbf{T} - a\mathbf{T}_v$, where the multiplying factor a secures that the eigenvalues of $\mathbf{T}_g$ is positive. This decomposition is known as the non-negative definite (NNED) Freeman-Durden decomposition.

Various alternative model-based decompositions have been proposed in the literature. The challenging part is the volume component. $\mathbf{T}_v$ is dependent on how the shape of the scattering elements are modeled, and on their orientation distribution [8]. Alternative volume scattering models have been proposed in the literature (see. e.g. [7, 8, 9]. For sea ice backscattering it is anticipated that depolarization can be caused by surface effects related to rough and highly deformed ice, as well as by volume type scattering from brine inclusions and inhomogenities inside the ice column. From previous analysis of polarimetric decompositions of sea ice scenes, we have seen that the power of the double bounce component often is an order of magnitude below the contribution from surface and volume scattering, and that high double bounce is restricted to isolated features. In this paper we present a recent, alternative model for the scattering coherence matrix, which only has only two terms, i.e.

$$\mathbf{T} = P_s\,\mathbf{T}_s + P_v\,\mathbf{T}_v, \tag{11}$$

where the surface component can contribute also to depolarization. Surface scattering is here imodelled by the extended Bragg model, or the X-Bragg model, described by Hainsek et al. in [8]. In the X-Bragg model the coherence matrix is given in the form of

$$\mathbf{T}_{XB} = \frac{1}{1+|\beta|^2}\begin{bmatrix} 1 & \gamma^* & 0 \\ \gamma & f_1(\delta) & 0 \\ 0 & 0 & f_2(\delta) \end{bmatrix}, \tag{12}$$

where $\gamma = \beta^* sinc(2\delta)$, $f_1(\delta) = \frac{1}{2}|\beta|^2(1 + sinc(4\delta))$, and $f_2(\delta) = \frac{1}{2}|\beta|^2(1 - sinc(4\delta))$. This model assumes a reflection symmetric depolarizer, where the Bragg coherency matrix is rotated

in the plane perpendicular to the scattering plane, and the $\mathbf{T}_{XB}$ is obtained as an average over the surface orientation angle distribution, assuming a uniform probability density function. The angle δ is here a measure of the width of this distribution, and accounts for the amount of roughness of the scattering surface. A smooth surface, on the scale of the radar wavelength, should have δ close to zero, whereas a rough and deformed ice surface should have a large δ. The β parameter is given as:

$$\beta = \frac{R_{hh} - R_{vv}}{R_{hh} + R_{vv}}, \tag{13}$$

where

$$R_{hh} = \frac{\cos\theta - \sqrt{\varepsilon_s - \sin^2\theta}}{\cos\theta + \sqrt{\varepsilon_s - \sin^2\theta}},$$

$$R_{vv} = \frac{(\varepsilon_s - 1)(\sin^2\theta - \varepsilon_s(1 + \sin^2\theta))}{(\cos\theta + \sqrt{\varepsilon_s - \sin^2\theta})},$$

θ is the incidence angle of the radar wave, and ε_s is the complex permittivity of the sea ice surface relating to salinity.

Combined with the X-Bragg surface scattering model, we will assume the volume scattering coherence matrix given in the form of

$$\mathbf{T}_V = \frac{1}{3-\rho}\begin{bmatrix} 1+\rho & 0 & 0 \\ 0 & 1-\rho & 0 \\ 0 & 0 & 1-\rho \end{bmatrix}. \tag{14}$$

The volume model assume randomly oriented scattering elements described by a shape parameter ρ. The shape parameter takes values between $\rho = 1/3$, corresponding to cylindrically shaped scatterers, to $\rho = 1$, corresponding to spherically shaped scatterers. This model has two contributions to the cross-polarzation power term, i.e T_{33}. In total the model has 5 unknowns, $P_v, P_s, \beta, \delta, \rho$, but only 4 independent equations to solve for the parameters. In previous applications of the X-Bragg model, authors have assumed one parameter fixed, and the solved for the others. We solve for the model parameters by adding high-order statical information. In this way, way can obtain a determined system of equations.

Figure 3 show images of the model parameters associated with the Radarsat 2 scene from the Fram Strait in 2011. The estimated parameters clearly display reasonable values of most of the parameters. We find strong surface contributions from the water, less from the levelled FY ice, and even less from more deformed MY ice. The δ-image on the upper right image indicates where we have smooth surfaces and more roughness. The water is and the levelled FY ice are fairly smooth areas, whereas the MY ice and the ridged ice clearly is found to be rough. Also the other parameter images show interesting features that are definitely associated with physical properties of the ice. For example, we would expect the water to have higher dielectric constant than the ice, but it is not so obvious that the ridged ice should have such a high β-value. The analysis and interpretation of these results is ongoing research.

RPAS SEA ICE MAPPING RESULTS

We will also include some preliminary results using Norut's Cryowing Micro RPAS for assessing the 3D structure of sea ice. The data was collected in the East of Svalbard during a scientific cruise with the Norwegian Coast Guard Vessel KV Svalbard in spring 2013.

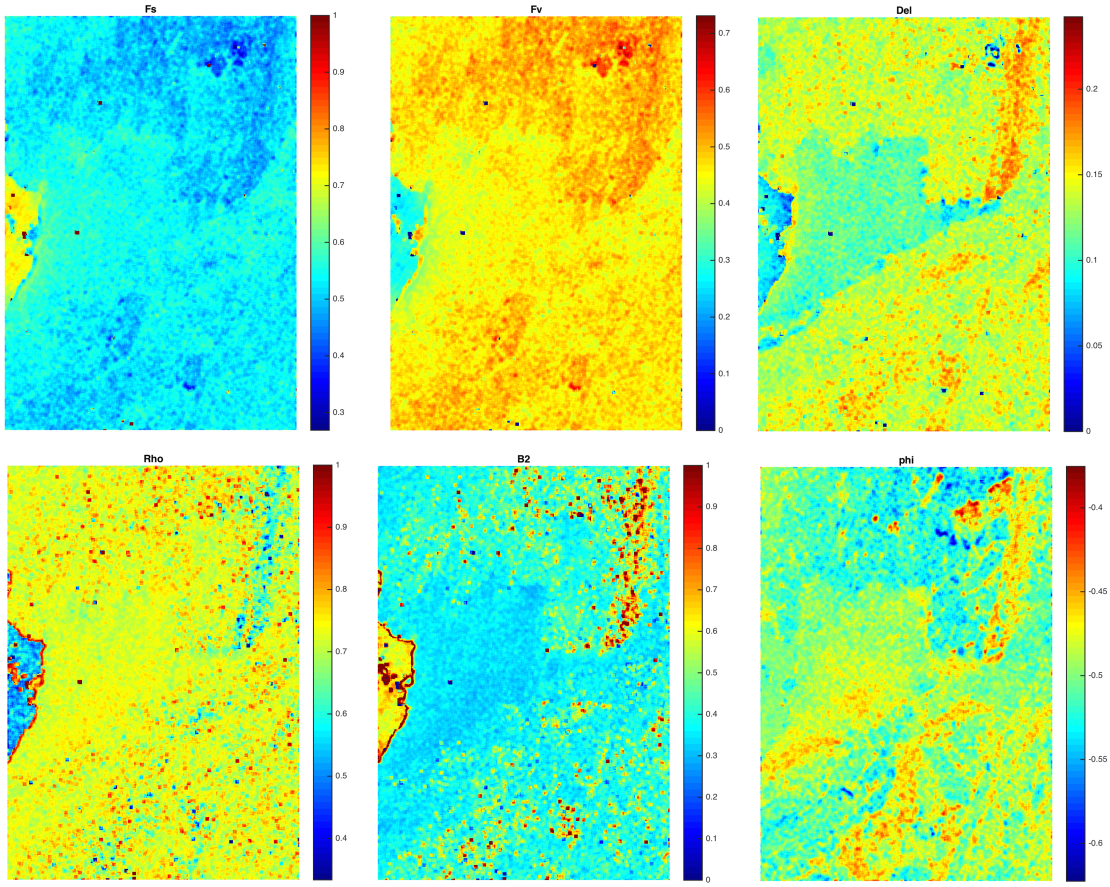

Figure 3. Images displaying estimated model-parameters fro the Fram Strait Radarsat 2 scene. *Upper panel left:* Relative surface contribution. *Upper panel middle:* Relative volume contribution. *Upper panel right:*Surface roughness δ. *Lower panel left:* Shape of volume scattering object ρ. *Lower panel middle:* Magnitude of $|\beta|^2$. *Lower panel right:* Angle of β.

A mosaic was generated by the Agisoft PhotoScan Pro software[1], and the 3D scene geometry was constructed using Structure-from-motion (SfM) approach [10, 11, 12]. Since the ice drifted about 1.5 m/s in S-SW direction during the flight, a GPS logging of the vessel's position was used to perform a first order correction on the aircraft position, to get the positions fixed relative to the sea ice. Further, all ground truth positions was marked on the ice with highly visible red markers. These ground control points where manually processed in order to further compensate for the ice-drift.The RPAS flight plan was set relative to the starting position, i.e. without using knowledge of the ice drift. In Figure 4, we observe the effect of this in the rather obscure area covered, which intuitively should be close to an rectangular grid.

In Figure 5, a close up of the pressure ridge of interest for the ground survey is shown, along with a rendered 3D view of the same ridge. We observe that the 3D model have some holes which are due to too few overlapping images, too uniform images/few features or open leads where the scene is not totally stationary. In the orthophoto, small holes have been filled by interpolating texture from the images onto a smooth surface.

[1] `www.agisoft.ru`

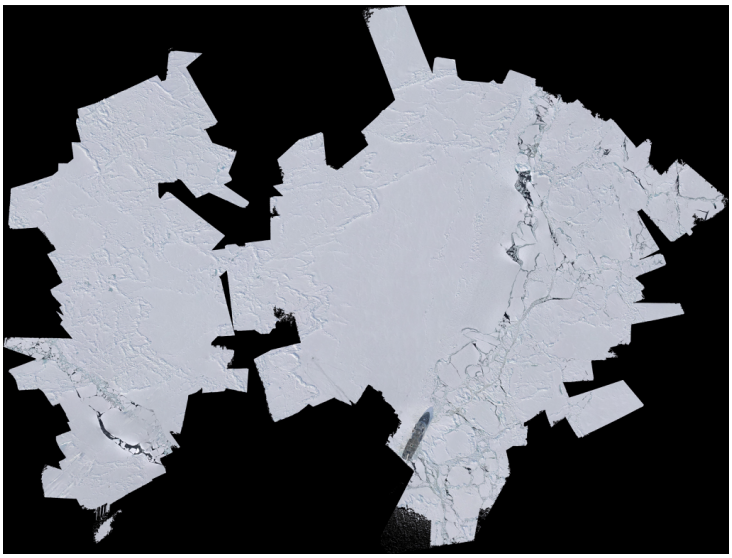

Figure 4. Orthophoto mosaic of the sea ice generated from a single flight with the Cryowing micro RPAS. Ground resolution is 5cm. The RPAS was deployed from the ship shown in the lower part of the image mosaic.

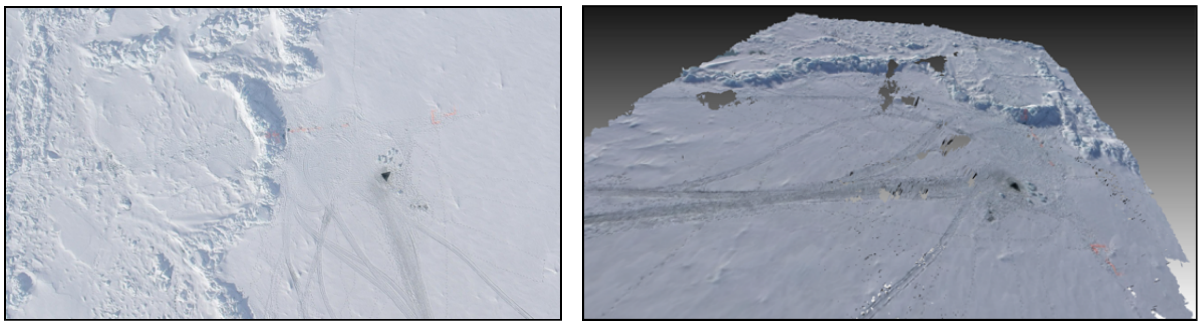

Figure 5. Closeup on the pressure ridge of interest (left) and corresponding rendered 3D model (right). Holes in the 3D model corresponds to areas where the SfM assumptions break down due to leads in the ice where the surface is not stationary on the timescale of the RPAS flight.

SUMMARY AND CONCLUSIONS

This paper demonstrates that resent developments in remote sensing technologies can provide information about sea ice structure. In the paper, we include some preliminaries on sea ice and radar polarimetry, and subsequently address segmentation, and strategies for analyses of polarimetric SAR data of sea ice. The analysis is conducted on a Radarsat 2 PolSAR scene of from the Fram Strait in September 2011. We show that the segmentation algorithm clearly enables segmentation of sea ice into proper segments, and some of these are easily identified as distinct ice types. The polarimetric parameters add information, which may allow to distinguish between ice classes of different roughness. We also include some preliminary results from a very recent model-based polarimetric decomposition approach, which uses higher-order statistics to estimate the model parameters. These results are very promising. We finally demonstrate that the sea ice surface structure may also be quite accurately mapped using RPAS technology. In future, this technology will be a valuable addition to satellite data for local mapping of the sea ice surface.

REFERENCES

[1] D. P. Winebrenner, D. G: Long, and B. Holt. *Mapping the progression of melt onset and the freeze-up on Arctic sea ice SAR and scatterometry.* Springer Verlag, Berlin, 1998.

[2] R. A. Schuchman, O. M. Johannessen R. O. Onsott, S. Sandven, and J. A. Johannessen. Processes at the ice edge the arctic. In *In "Synthetic Aperture Radar Marine User's Manual." Eds. C. R. Jackson and J. R. Apel*, Washington, DC, 2004. National Oceanic Atmospheric Administration.

[3] J-S Lee and E. Pottier. *Polarimetric Radar Imaging, from basics to applications*. Taylor & Francis Group, 2009.

[4] Shane R. Cloude. *Polarisation: Applications in Remote Sensing*. Oxford University Press, Oxford, UK, 2010.

[5] W.-M. Boerner. Basic concepts in radar polarimetry. Technical report, UIC-ECE Communications, Sensing & Navigation Laboratory, Chicago, IL/USA, 2010.

[6] A.P. Doulgeris and T. Eltoft. Polsar image segementation - advanced statistical modelling versus simple feature extraction. Proc. IGARSS 2014.

[7] Anthony Freeman and Stephen L. Durden. A three-component scattering model for polarimetric SAR data. *IEEE Trans. Geosci. Remote Sens*, 36(3):963–973, May 1998.

[8] I. Hajnsek, T. Jagdhuber, H. Schön, and K. P. Papathanassiou. Potensial of estimating soil moisture under vegetation cover by means of polsar. *IEEE Trans. Geosci. Remote Sens*, 47(2):442–454, 2009.

[9] W. An, Y. Cui, and J. Yang. Three-component model-based decomposition for polarimetric SAR data. *IEEE Trans. Geosci. Remote Sens*, 48(6):2732–2739, 2010.

[10] S. Ullman. The interpretation of structure from motion. *Proc. R. Soc. Lond. B*, 203:405–426, 1979.

[11] N. Snavely, S.M. Seitz, and R. Szeliski. Photo tourism: Exploring photo collections in 3D. *ACM Trans. Graph.*, 25:835–846, 2006.

[12] M.J. Westoby, J. Brasington, N.F. Glasser, M.J Hambrey, and J.M. Reynolds. "Stucture-from-Motion" photogrammetry: A low-cost, effective tool for geoscience applications. *Geomorphology*, 179:300–314, 2012.